Crystallization study by transmission electron microscopy of SrTiO3 thin films prepared by plasma-assisted ALD

ECS Journal of Solid State Science and Technology, **2** (5) N120-N124 (2013)
2162-8769/2013/2(5)/N120/5/$31.00 © The Electrochemical Society

Crystallization Study by Transmission Electron Microscopy of $SrTiO_3$ Thin Films Prepared by Plasma-Assisted ALD

V. Longo,[z] M. A. Verheijen, F. Roozeboom,[*] and W. M. M. Kessels[*,z]

Department of Applied Physics, Eindhoven University of Technology, 5600 MB Eindhoven, The Netherlands

The crystallization behavior of thin strontium titanate ($SrTiO_3$, STO) films with ~15 nm thickness was studied by Transmission Electron Microscopy (TEM). Amorphous STO films with [Sr]/([Sr]+[Ti]) ratio ranging from 0.50 to 0.63 were deposited at 350°C by plasma-assisted ALD and subsequently treated by rapid thermal annealing in flowing N_2 for crystallization. Different temperatures and annealing durations were employed to fully characterize the crystallization process. TEM analysis showed that transrotational crystals were formed and evidenced the influence of the STO composition and of the thermal budget applied on the grain size, crack and void formation. In particular, Sr-rich layers ([Sr]/([Sr]+[Ti] ≥ 0.59) showed a finer crystalline structure which was imputed to a higher nucleation probability at the onset of the crystallization process. Crystallization into the perovskite structure was confirmed for all the film compositions studied. By tuning the STO composition and the thermal budget of the annealing step it was demonstrated that it is possible to control the microstructure of the crystallized film as a further step in optimizing the STO film properties.
 [DOI: 10.1149/2.016305jss]

Manuscript submitted February 8, 2013; revised manuscript received March 8, 2013. Published March 21, 2013. This was Paper 2462 presented at the Honolulu, Hawaii, Meeting of the Society, October 7–12, 2012.

Strontium titanate ($SrTiO_3$, STO) has received a lot of attention due to its properties that are related to its perovskite crystal structures. Among these, ferro-electricity, para-electricity, resistive-switching behavior and oxygen sensing have been reported for thin STO layers deposited by various techniques, such as physical vapor deposition (PVD), chemical vapor deposition (CVD) and pulsed laser deposition (PLD).[1–9] Furthermore STO is an *ultrahigh-k* material with a theoretical *k*-value ~300 for bulk STO. This property combined with a good thermal stability and relatively low crystallization temperature makes STO the dielectric material of choice for next generation dynamic random access memories (DRAM).[10–12] STO *high-k* dielectric films have been deposited by ALD, especially since the application in deep trenches in silicon wafers calls for extremely conformal layers in such 3D structures. As ALD is the preferred technology of choice, the thermal budget used during the deposition needs to be limited to prevent decomposition of the metal-organic precursors typically employed. At low deposition temperatures the as-deposited STO films are amorphous and a thermal treatment is required to crystallize the films afterwards in order to obtain STO with the high dielectric constant targeted. Crystallization into the perovskite structure is achieved also for non-stoichiometric STO thin films. It has been shown that excess Sr is accommodated in the crystalline STO in a solid solution and it is only expelled out of the STO grains during high temperature annealing (>700°C).[13,14] Increasing the Sr-content results in lower *k*-values compared to the stoichiometric films.[15–17] However, Sr-rich layers are to be used in next generation DRAM due to their superior dielectric properties and microstructure leading, amongst others, to lower leakage currents.[10,11]

The thermal budget applied during annealing as well as specific parameters such as film composition and thickness are of crucial importance as they determine the crystallization behavior and the consequent final microstructure and electrical properties of the crystallized STO films. Crystallization of the film leads to in-plane and out-of-plane densification of the film. Because of the in-plane directional crystal growth, densification will eventually lead to void formation. Depending on the density of nuclei, the growth morphology and rate, voids will be either homogeneously distributed or concentrated at the grain boundaries, the latter leading to networks of so-called 'nano-cracks'.[14] These lower density regions are detrimental if the STO is employed as a dielectric material. The cracks at the grain boundaries can be either formed due to densification caused by solid-state diffusion or to tensile stress between grains.[13,14] Recent studies showed that, when crystallized, Sr-rich layers ([Sr]/([Sr]+[Ti]) = 0.62) develop a smaller grain size than stoichiometric films. This finer microstructure results in reduced crack formation, thus improved leakage current performance and dielectric properties.[10–13,18] This example shows the importance of resolving the correct process and temperature window to obtain the desired film properties for the specific application targeted. In recent literature, TEM studies have been published on STO films deposited by ALD and crystallized by rapid thermal annealing (RTA) with the aim of determining the STO microstructure and its relation to electrical properties.[13,14,18,19] However, to date a comprehensive study has not been reported on the relation between film composition, thermal budget and the crystalline microstructure of thin STO films. Since STO thin films are likely candidates for the above-mentioned applications, an in-depth understanding of their crystallization behavior will be vital.

In this work, we report on the crystallization behavior of STO thin films deposited by plasma-assisted ALD. The microstructure of the thin crystallized films was studied by TEM. To investigate the eventual influence of the underlying surface on the crystallization behavior, the 15 nm thin STO films were deposited at 350°C both on bare Si_3N_4 and on Al_2O_3-coated Si_3N_4 TEM windows. These two materials show good diffusion barrier properties and remain in the amorphous state for the annealing temperatures employed in this work. This makes them both suitable for TEM imaging. Furthermore, Al_2O_3 is commonly used as a leakage current barrier layer in capacitor structures such as the one employed in DRAM technology.[20] Films with different compositions were treated by RTA. Different annealing temperatures and durations were applied to characterize the successive steps in the nucleation and crystallization. TEM analysis revealed that the temperature, the anneal duration and the film composition influence the final microstructure of the crystalline STO films. In particular it was shown that by accurately choosing the above mentioned parameters it is possible to control the average size and the morphology of the grains.

Experimental

STO thin films of nominal 15 nm thickness were deposited in an Oxford Instruments FlexAL thermal and plasma ALD reactor. The layers were deposited by plasma-assisted ALD at a temperature set at 350°C. The precursors employed were Ti-Star, (pentamethylcyclopentadienyl)trimethoxy-titanium, $CpMe_5Ti(OMe)_3$, and Hyper-Sr, bis(tri-isopropylcyclopentadienyl) strontium with 1,2-dimethoxyethane adduct, $Sr(^iPr_3Cp)_2DME$, both from AirLiquide. An O_2 (>99.999% purity) plasma generated by an inductively coupled plasma (ICP) source was used as the oxidizing agent. STO was obtained by mixing ALD cycles of the binary oxides TiO_2 and SrO. The details of the ALD process are reported elsewhere.[21,22] Films were deposited employing different [SrO]/[TiO_2] ALD cycle ratios to obtain different film

*Electrochemical Society Active Member.
[z]E-mail: v.longo@tue.nl; W.M.M.Kessels@tue.nl

Table I. [SrO]/[TiO_2] ALD cycle ratio, thickness and [Sr]/([Sr]+[Ti]) ratio of the STO films analyzed by TEM. The thickness and the [Sr]/([Sr]+[Ti]) ratio of the films in the as-deposited state were determined from spectroscopic ellipsometry experiments.[22] The errors in thickness and in the [Sr]/([Sr]+[Ti]) ratio are ±0.50 nm and ±0.03, respectively.

[SrO]/[TiO_2] ALD cycle ratio	Thickness (nm)	[Sr]/([Sr]+[Ti]) Ratio
1:3	15.8	0.50
2:5 mixed*	15.4	0.53
1:2	14.9	0.59
2:3	15	0.63

*In the "*mixed*" approach TiO_2 and SrO ALD cycles were intermixed (i.e. the [SrO]/[TiO_2] ALD cycle ratio = 2:5 mixed corresponds to the sequence 1 SrO, 2 TiO_2, 1 SrO and 3 TiO_2 cycles).[21,22]

compositions.[21,22] Silicon substrates were placed adjacent to the TEM windows (13 nm Si_3N_4 membranes) inside the reactor chamber during the depositions to allow ex-situ spectroscopic ellipsometry (SE) measurements (M2000D, J.A. Woollam, 1.25–6.5 eV). The elemental composition was extracted from the ellipsometry data by means of an optical constant library which was calibrated by means of Rutherford backscattering experiments.[21] The [SrO]/[TiO_2] ALD cycle ratios, the thicknesses in the as-deposited state and the [Sr]/([Sr]+[Ti]) ratios of the films examined in this study are listed in Table I.

RTA in flowing N_2 was performed in an AST SHS100 system at temperatures ranging from 550°C to 650°C to crystallize the STO films. To determine the influence of the annealing duration, RTA was conducted for different dwell times for samples having the same STO layer deposited. For this purpose, the duration of the initial temperature ramp to reach the set RTA temperature was kept constant for samples annealed at the same temperature (10 s for 550°C, 15 s for 600°C and 650°C), only the dwell time for the set temperature was varied. TEM studies were performed using a TECNAI F30ST TEM operated at 300 kV. Both Bright-Field TEM (BF-TEM) and High Angle Annular Dark-Field Scanning TEM (HAADF-STEM) modes were employed to characterize the samples. X-ray diffractometry (XRD) was performed on a Panalytical X'Pert PRO MRD employing Cu K_α (0.154 nm) radiation to determine the crystalline phase of the annealed films. Atomic Force Microscopy (AFM) was employed to study the surface morphology. AFM scans were performed using a NT-MDT Solver P47 microscope. Samples were scanned in tapping mode using a TiN coated Si tip (NSG10/TiN, NT-MDT).

Results and Discussion

Figures 1a–1c show Bright Field-TEM (BF-TEM) images of STO films on Si_3N_4 windows with [Sr]/([Sr]+[Ti]) = 0.53 annealed at 550°C for different times. The sample annealed for 1 minute was mainly amorphous containing only a low density of nuclei that can be recognized as darker dots in Figure 1a. Upon annealing the film for 5 minutes, many crystals have formed in the amorphous matrix. Each crystal has its origin in a single-crystalline nucleus that grows due to solid state crystallization expanding in the amorphous matrix. The different sizes of the crystals can be explained by a crystallization process with a constant growth rate, where new nuclei are continuously formed during the crystallization process. After 10 minutes the layer was still not completely crystallized due to the slow crystal growth rate (<0.1 μm/min) obtained under these conditions. In our study we can distinguish between two crystallization regimes: *nucleation-dominated* and *growth-dominated*. In the first, the nucleation probability is high, leading to a high density of small crystals that are limited in their lateral growth by the proximity of other nuclei, resulting in a small average crystal size upon full crystallization. In the latter, the nucleation probability is low and the crystallization process is dominated by growth of a low density of crystals, leading

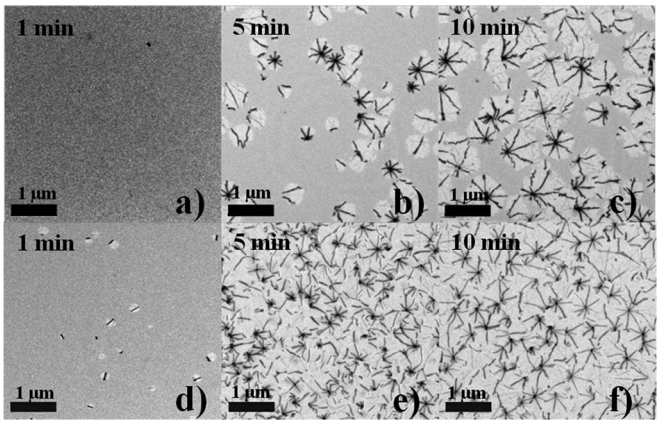

Figure 1. BF-TEM images of STO films on Si_3N_4 windows with [Sr]/([Sr]+[Ti]) = 0.53 (a-c) and [Sr]/([Sr]+[Ti]) = 0.59 (d-f) after RTA at 550°C for different annealing times as indicated in the figure.

to a large crystal size upon full crystallization. A similar distinction of the two crystallization regimes can be found in the literature for phase change materials.[23] In case of the above mentioned 550°C anneal and [Sr]/([Sr]+[Ti]) = 0.53, the crystallization is *growth-dominated* rather than *nucleation-dominated*, resulting in an average grain size of 1 μm once the layer is fully crystallized.

Figures 1d–1f show BF-TEM images of STO films on Si_3N_4 windows having [Sr]/([Sr]+[Ti]) = 0.59 annealed at 550°C for different times. For this increased Sr-content in the STO film more nuclei can be observed for the sample annealed for 1 minute. This indicates that Sr-rich layers have a higher nucleation probability than the more stoichiometric ones. In addition, Sr-rich films exhibit a higher growth rate for the crystallites, resulting in a fully crystallized film already for an annealing time of 5 minutes. A further increase to 10 minutes did not result in remarkable morphological changes. The higher density of nuclei, compared to the film with [Sr]/([Sr]+[Ti]) = 0.53, resulted in a final smaller average grain size (~0.5 μm). The STO film with [Sr]/([Sr]+[Ti]) = 0.63 (data not shown) was also fully crystalline after a 5 minutes anneal at 550°C and showed an even smaller grain size (<0.2 μm) while the STO film with [Sr]/([Sr]+[Ti]) = 0.50 (data not shown) was fully amorphous after 1 minute RTA at 550°C thus showing the lowest nucleation probability among the four compositions. Similar results were obtained for the STO films deposited on the Al_2O_3-coated windows.

The star-shaped patterns of varying diffraction contrast that can be recognized in the reported BF-TEM images are an indication of bending of the lattice planes within a single crystal. The term *transrotational crystals* was introduced by Kosolov et al. to describe this particular crystalline structure, since the lattice planes are not only replicated or *translated* but also *rotated* during crystal growth.[24] While grains in polycrystalline thin films give a uniform contrast in TEM imaging depending on their crystal orientation, transrotational crystals show contrast patterns due to the lateral variation in crystal orientation. The internal lattice plane bending is due to stress induced by the amorphous-to-crystalline transformation and film densification.[23,24] In the work of Kooi et al. it was proposed that, during crystal growth, new crystal planes nucleate at the top interface and the crystal front is characterized by a thickness profile with the crystallized region being thinner than the surrounding amorphous matrix. With the crystal expanding the crystal front advances and these newly formed crystal planes are "pushed down", resulting in internal lattice bending.[23] This hypothesis is consistent with the SE measurements performed before and after full crystallization of the STO films where a thickness reduction of ~15% was recorded upon crystallization. Figure 2a shows an AFM topography image of an STO film with [Sr]/([Sr]+[Ti]) = 0.53 annealed at 550°C for 5 minutes. In Figure 2a the developing transrotational crystals are visible as disk-shaped regions with a diameter

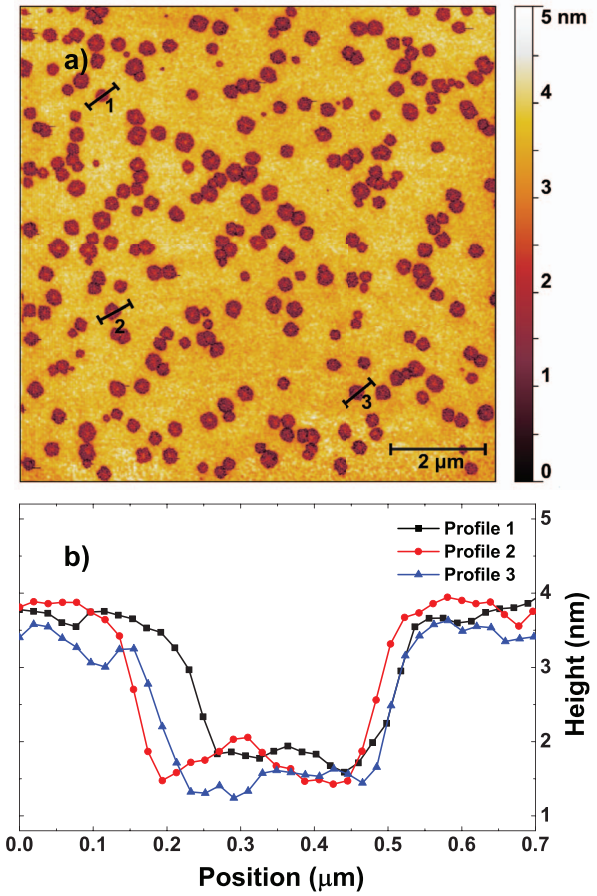

Figure 2. 10 µm × 10 µm AFM scan of a STO film deposited on a bare Si_3N_4 TEM window with [Sr]/([Sr]+[Ti]) = 0.53 after RTA at 550°C for 5 minutes (a) and height profiles along the three different developing crystals indicated in the AFM image (b).

of ∼300 nm and with a decreased thickness compared to the amorphous regions. Grain size and distribution are in excellent agreement with TEM images of samples with the same processing conditions (Figure 1b). Figure 2b displays the height profile along three different paths marked in Figure 2a, each one crossing different single developing crystallites. The thickness difference between the crystallized and the amorphous STO is in the range of 2–2.5 nm, which is in good agreement with the decrease in thickness detected by SE. These measurements are also in good agreement with the model proposed by Kooi et al. where a thickness gradient is assumed at the crystal front.[23]

The star-shaped bending contours show mainly a 3-fold or a 4-fold symmetry corresponding to specific crystallographic orientations. In particular, the center of the star corresponds to a zone axis and the symmetry of the branches depends on the orientation of the zone axis. In particular a ⟨001⟩ and a ⟨111⟩ zone axis will show a 4-fold or a 3-fold symmetry, respectively. In this configuration, the crystal planes nearly perpendicular to the film surface giving rise to the bending contours are the planes oriented perpendicular to the orientation of the zone axis. Favia et al. performed nano-beam diffraction (NBD) on the center and on the branches of stars with 4-fold symmetries that formed after crystallization of thin STO films.[25] Their analysis evidenced that the center of the star corresponds to a ⟨001⟩ zone axis. NBD performed on the branches of the star showed diffraction patterns displaying periodicity in only one in-plane direction, implying that the bending contour contrast along a branch of the star originates from only one set of crystal planes.

Figures 3a–3d and 3e–3h show High Angle Annular Dark-Field Scanning TEM (HAADF-STEM) images of STO films with different

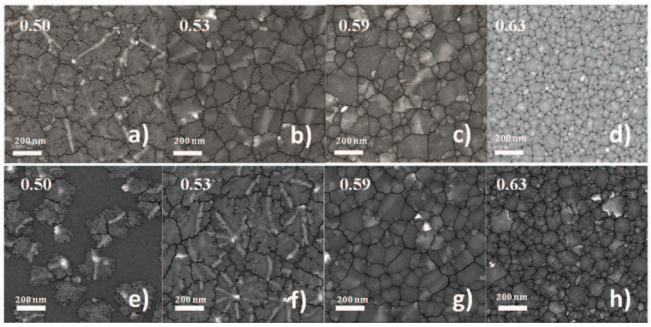

Figure 3. HAADF-STEM images of STO films with [Sr]/([Sr]+[Ti]) ratios ranging between 0.50 and 0.63 deposited on Al_2O_3-coated (a-d) and bare Si_3N_4 (e-h) TEM windows and annealed by RTA at 600°C for 1 minute.

[Sr]/([Sr]+[Ti]) ratios deposited on Al_2O_3-coated and bare Si_3N_4 windows, respectively, annealed by RTA at 600°C for 1 minute. For these studies, HAADF-STEM imaging was preferred over BF-TEM imaging because of the excellent visibility of low-density regions (voids, nano-cracks). Instead of using a low camera length creating pure *Z* (atomic number) contrast, an intermediate camera length was selected to visualize both density differences as well as diffraction contrast. All layers were completely crystalline except for the STO film with [Sr]/([Sr]+[Ti]) = 0.50 deposited on Si_3N_4. A slightly lower nucleation probability was found for layers deposited on bare windows. Independently of the substrate, the microstructure of the crystallized films was found to have the same trend depending on the film composition. In particular, an increased Sr-content resulted in a smaller grain size, similar to the results obtained at 550°C (Figure 1e–1f). This suggests that also for annealing at 600°C Sr-rich layers show a higher nucleation probability. Both the average size and the morphology of the crystallites changed with composition. For near-stoichiometric compositions ([Sr]/([Sr]+[Ti]) = 0.50, 0.53) (Figures 3a and 3b, 3e and 3f) the grains have a dendritic morphology with voids situated predominantly between the merging dendritic branches. The crystals have formed trans-rotationally with visible bending contours (white lines). For [Sr]/([Sr]+[Ti]) = 0.59 (Figures 3c, 3g), the crystallites showed a more regular shape. In addition, the bending contours within the grains are broader compared those which were visible for the more stoichiometric STO films, implying a reduced curvature of the crystal lattice. Kolosov et al., and Kooi et al. reported reduced internal bending for higher crystal growth rates.[23,24] This indicates that Sr-rich STO shows a higher nucleation probability as well as an increased crystal growth rate. For films with the highest Sr-content ([Sr]/([Sr]+[Ti]) = 0.63, (Figures 3d and 3h) the average grain size is further decreased and the bending contours related to the transrotational structure are no longer present.

Figure 4a–4d shows high magnification HAADF-STEM images of the samples with different compositions deposited on Al_2O_3-coated windows (cf. Figures 3a–3d). For near-stoichiometric films ([Sr]/([Sr]+[Ti]) = 0.50, 0.53) nano-cracks were formed at the grain boundaries and voids (black dots) with a diameter of a few nanometers were found within the crystals. For increased Sr-content ([Sr]/([Sr]+[Ti]) = 0.59) the voids were only present at the grain boundaries while small pores (>1nm) within the grain appeared. The

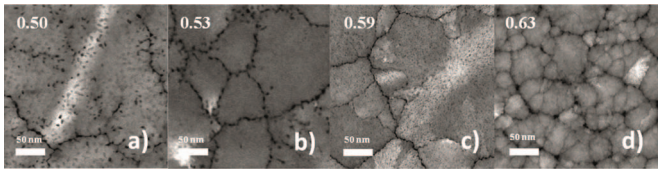

Figure 4. High magnification HAADF-STEM images of STO films with [Sr]/([Sr]+[Ti]) ratios ranging between 0.50 and 0.63 deposited on Al_2O_3-coated TEM windows and annealed by RTA at 600°C for 1 minute.

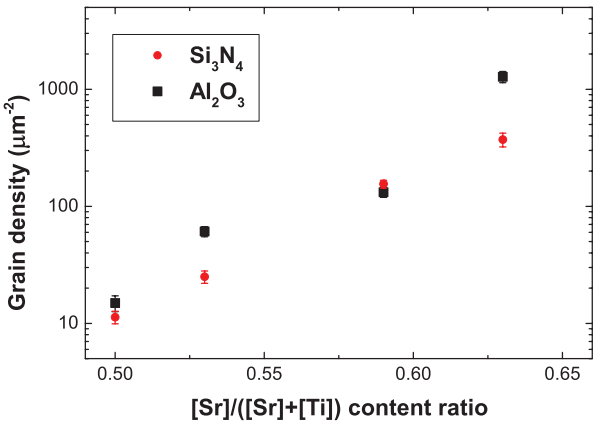

Figure 5. Grain density of STO films deposited on bare Si_3N_4 and Al_2O_3-coated TEM windows with different [Sr]/([Sr]+[Ti]) content ratios after RTA for 1 minute at 600°C.

film with [Sr]/([Sr]+[Ti]) = 0.63 showed a similar microstructure with voids formed between clusters of grains with even smaller average size. These higher resolution images also revealed changes in the structure of the grain boundaries. Well defined single grains separated by nano-cracks could be identified for near-stoichiometric layers. The films with increased Sr-content are characterized by clusters of closely packed crystals separated by voids.

Figure 5 shows the grain density of STO films deposited on the bare and Al_2O_3-coated Si_3N_4 TEM windows upon a 1 minute RTA anneal at 600°C. For both substrates the trend was similar: an exponential increase in grain density as a function of Sr-content was found in the compositional range studied. As shown in Figure 3, this increase in grain density is due to a transition from *growth-dominated* to *nucleation-dominated* in the crystallization process when the Sr-content is increased. On both substrates an average grain size of ~50 nm was found for the films with a [Sr]/([Sr]+[Ti]) ratio of 0.63. This is in good agreement with literature results for STO layers with [Sr]/([Sr]+[Ti]) = 0.62 deposited on TiN.[13,14] Apart from the film on Si_3N_4 with [Sr]/([Sr]+[Ti]) = 0.50 (50% crystalline) all samples were fully crystalline after 1 minute RTA.

Figure 6a shows the influence of the RTA temperature on the grain for STO films with [Sr]/([Sr]+[Ti]) = 0.53. Higher anneal temperatures lead to an increased nucleation probability and, consequently a higher grain density. In particular, the annealing temperature range from 550°C to 650°C results in a difference of more than two orders of magnitude in the grain density. It should be noted that an RTA of 1 minute at 550°C only yields a low degree of crystallinity, as shown in Fig. 1a. Figure 6b shows the evolution of the grain density over annealing time for the RTA at 550°C. A grain density of ~3 μm^{-2} was achieved for both substrates after 10 minutes leading to nearly fully crystallized layers (Fig. 1c). This grain density is nearly one order of magnitude lower as compared to higher temperature anneals illustrating the difference between the *growth-dominated* crystallization process at 550°C and the *nucleation-dominated* crystallization at higher annealing temperatures.

GI-XRD was performed on STO films with [Sr]/([Sr]+[Ti]) = 0.53 and 0.63 deposited on Si samples coated with 20 nm Al_2O_3 to determine the crystalline structure after RTA. This substrate was used since GI-XRD on TEM windows was not possible due to size restrictions. The GI-XRD spectra of STO film after RTA with different thermal budgets with [Sr]/([Sr]+[Ti]) = 0.53 and 0.63 are shown in Figure 7b and 7c. The STO film with [Sr]/([Sr]+[Ti]) = 0.53 annealed

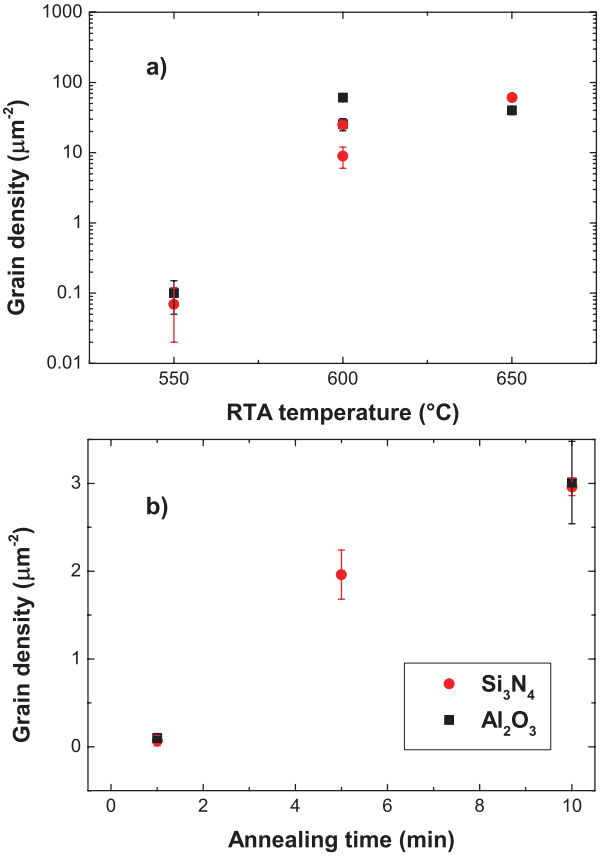

Figure 6. Grain density of STO films with [Sr]/([Sr]+[Ti]) = 0.53 on bare and Al_2O_3-coated Si_3N_4 TEM windows after RTA for 1 minute at annealing temperatures ranging from 550°C to 650°C (a) and its evolution over annealing time for the RTA at 550°C (b).

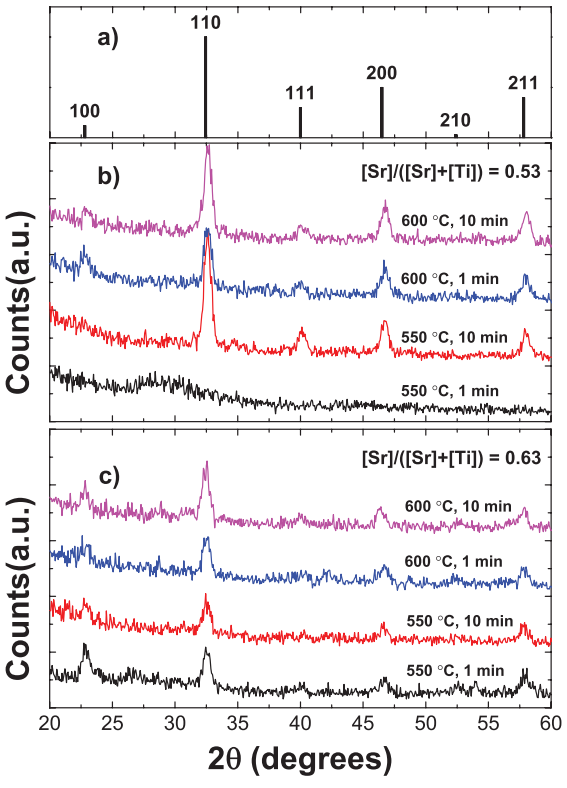

Figure 7. The diffraction spectrum for the $SrTiO_3$ perovskite structure[26] reported as a reference (a) for the GI-XRD spectra of STO films with [Sr]/([Sr]+[Ti]) = 0.53 (b) and 0.63 (c) deposited on 20 nm Al_2O_3/Si samples after RTA at 550°C and 600°C for 1 and 10 minutes.

at 550°C for 1 minute was amorphous. Increasing the RTA time to 10 minutes resulted in the full crystallization of the layer. This is in agreement with the TEM results reported above (Figure 1a–1c) where only a few nuclei were formed at this temperature after 1 minute RTA. The film with [Sr]/([Sr]+[Ti]) = 0.63 was fully crystalline after 1 min RTA at 550°C. This confirms that for higher Sr-content a higher degree of crystallization is achieved compared to the more stoichiometric STO films. No remarkable difference was found between the GI-XRD spectra of the Sr-rich films for the different thermal budgets applied. This suggests that for this composition, the film is rapidly crystallized and a comparable microstructure is achieved due to a high nucleation probability at both temperatures.

Regardless of the film composition, only diffraction peaks corresponding to the STO perovskite structure were detected.[26] For the film with [Sr]/([Sr]+[Ti]) = 0.63 the diffraction peaks shifted to lower angles. This suggests that, for the annealing temperatures employed in this work, the excess of Sr is not segregating, but accommodated in the perovskite structure resulting in an expansion of the unit cell parameter. Menou et al. reported a similar shift of the diffraction peaks due to increased Sr-content in the STO film.[13] In the same work, it was also shown that no Ruddlesden-Popper phases were observed for annealing temperature up to 700°C.[13] It was suggested that the excess Sr was in solution in the perovskite structure and that the Sr was only expelled out of the grains for high annealing temperatures (>700°C).

Conclusions

The influence of the thermal budget applied during rapid thermal annealing and of the elemental composition on the crystallization behavior of thin STO films deposited by plasma-assisted ALD was investigated. The grain size and crystallite density strongly depend on the film composition in the compositional range examined (([Sr]/([Sr]+[Ti]) from 0.50 to 0.63) with a decreasing grain size achieved when more Sr is incorporated in the layer. This was imputed to the higher nucleation probability for Sr-rich layers. This trend was found to be independent of the substrate used (Si_3N_4 or Al_2O_3). The nucleation probability appears to exhibit a stronger temperature dependency than the crystal growth rate, leading to a higher grain density, i.e. smaller grain size, at higher annealing temperatures. Furthermore, the microstructure of the films and the distribution of the voids within one single crystal and of nano-cracks at the grain boundaries were found to be dependent on the film stoichiometry. Nearly stoichiometric films ([Sr]/([Sr]+[Ti]) = 0.50, 0.53) showed transrotational crystals with voids formed within the single grains and nano-cracks at the grain boundaries. The bending of the lattice planes was reduced for higher Sr-contents due to the higher crystal growth rate. Increasing the Sr-content resulted in a smaller size of the pores formed within one single crystallite (<1 nm for ([Sr]/([Sr]+[Ti]) = 0.59 and 0.63) and in a more compact microstructure. We demonstrated that by choosing the thermal budget applied during the annealing step as well as the film composition it is possible to change the grain size, crystallites morphology and the distribution of voids and cracks. With these insights, these parameters can be tailored to obtain the microstructure which is most suitable for the specific application in which the STO film is used.

Acknowledgments

This research was funded by the European Community's Seventh Framework Program (FP7/2007-2013) under grant agreement number ENHANCE-238409. The authors thank W. Keuning for the GI-XRD measurements, C.A.A van Helvoirt for the technical support and A. Zauner (Air Liquide) for providing the precursors. The research of W.M.M. Kessels is supported by the Netherlands Organization for Scientific Research (NWO) and the Technology Foundation STW through the project on "Nanomanufacturing".

References

1. R. Wödenweber, E. Hollmann, M. Ali, J. Schubert, G. Pickartz, and T. K. Lee, *J. Eur. Ceram. Soc.*, **27**, 2899 (2007).
2. Y. S. Kim, D. J. Kim, T. H. Kim, T. W. Noh, J. S. Choi, B. H. Park, and J.-G. Yoon, *Appl. Phys. Lett.*, **91**, 042908 (2007).
3. D. Marré, A. Tumino, E. Bellingeri, I. Pallecchi, L. Pellegrino, and A. S. Siri, *J Phys. D Appl. Phys.*, **36**, 896 (2003).
4. F. M. Pontes, E. J. H. Lee, E. R. Leite, and E. Longo, *J. Mater. Sci.*, **35**, 4783 (2000).
5. R. Muenstermann, T. Menke, R. Dittmann, S. Mi, C.-L. Jia, D. Park, and J. Mayer, *J. Appl. Phys.*, **108**, 124504 (2010).
6. K. Szot, R. Dittmann, W. Speier, and R. Waser, *Phys. Status Solidi RRL*, **1**, R86 (2007).
7. X. B. Yan, Y. D. Xia, H. N. Xu, X. Gao, H. T. Li, R. Li, J. Yin, and Z. G. Liu, *Appl. Phys. Lett.*, **97**, 112101 (2010).
8. T. Hara and T. Ishiguro, *J. Ceram. Soc. Jpn.*, **118**, 300 (2010).
9. T. Hara and T. Ishiguro, *Sensor. Actuat. B- Chem.*, **136**, 489 (2009).
10. M.-S. Kim, M. Popovici, J. Swerts, M. A. Pawlak, K. Tomida, B. Kaczer, K. Opsomer, M. Schaekers, H. Tielens, C. Vrancken, S. van Elshocht, I. Debusschere, L. Altimime, and J. A. Kittl, *3rd IEEE International Memory Workshop* (2011).
11. M. A. Pawlak, M. Popovici, J. Swerts, K. Tomida, M.-Soo Kim, B. Kaczer, K. Opsomer, M. Schaekers, P. Favia, H. Bender, C. Vrancken, B. Govoreanu, C. Demeurisse, W.-Chih Wang, V. V. Afanas'ev, I. Debusschere, L. Altimime, and J. A. Kittl, IEDM 2010.
12. M. A. Pawlak, B. Kaczer, M.-S. Kim, M. Popovici, J. Swerts, W.-C. Wang, K. Opsomer, P. Favia, K. Tomida, A. Belmonte, B. Govoreanu, C. Vrancken, C. Demeurisse, H. Bender, V. V. Afanas'ev, I. Debusschere, L. Altimime, and J. A. Kittl, *Appl. Phys. Lett.*, **98**, 182902 (2011).
13. N. Menou, M. Popovici, S. Clima, K. Opsomer, W. Polspoel, B. Kaczer, G. Rampelberg, K. Tomida, M. A. Pawlak, C. Detavernier, D. Pierreux, J. Swerts, J. W. Maes, D. Manger, M. Badylevich, V. V. Afanas'ev, T. Conard, P. Favia, H. Bender, B. Brijs, W. Vandervorst, S. van Elshocht, G. Pourtois, D. J. Wouters, S. Biesemans, and J. A. Kittl, *J. Appl. Phys.*, **106**, 094101 (2009).
14. M. A. Pawlak, B. Kaczer, M.-S. Kim, M. Popovici, K. Tomida, J. Swerts, K. Opsomer, W. Polspoel, P. Favia, C. Vrancken, C. Demeurisse, W.-C. Wang, V. V. Afanas'ev, W. Vandervorst, H. Bender, I. Debusschere, L. Altimime, and J. A. Kittl, *Appl. Phys. Lett.*, **97**, 162906 (2010).
15. S. Clima, G. Pourtois, N. Menou, M. Popovici, A. Rothschild, B. Kaczer, S. van Elshocht, X. P. Wang, J. Swerts, D. Pierreux, S. De Gendt, D. J. Wouters, and J. A. Kittl, *Microelectron. Eng.*, **86**, 1936 (2009).
16. S. K. Kim, S. W. Lee, J. H. Han, B. Lee, S. Han, and C. S. Hwang, *Adv. Func. Mat.*, **20**, 2989 (2010).
17. M. Popovici, S. van Elshocht, N. Menou, J. Swerts, D. Pierreux, A. Delabie, B. Brijs, T. Conard, K. Opsomer, J. W. Maes, D. J. Wouters, and J. A. Kittl, *J. Electrochem. Soc.*, **157**, G1 (2010).
18. M. Popovici, S. van Elshocht, N. Menou, P. Favia, H. Bender, E. Rosseel, J. Swerts, C. Adelmann, C. Vrancken, A. Moussa, H. Tielens, K. Tomida, M. Pawlak, B. Kaczer, G. Schoofs, W. Vandervorst, D. J. Wouters, and J. A. Kittl, *J. Vac. Sci. Technol. B*, **29**, 01A304 (2011).
19. P. Favia, M. Popovici, G. Eneman, G. Wang, M. Bargallo-Gonzalez, E. Simoen, N. Menou, and H. Bender, *ECS Trans.*, **33**(11), 205 (2010).
20. J. A. Kittl, K. Opsomer, M. Popovici, N. Menou, B. Kaczer, X. P. Wang, C. Adelmann, M. A. Pawlak, K. Tomida, A. Rothschild, B. Govoreanu, R. Degraeve, M. Schaekers, M. Zahid, A. Delabie, J. Meersschaut, W. Polspoel, S. Clima, G. Pourtois, W. Knaepen, C. Detavernier, V. V. Afanas'ev, T. Blomberg, D. Pierreux, J. Swerts, P. Fischer, J. W. Maes, D. Manger, W. Vandervorst, T. Conard, A. Franquet, P. Favia, H. Bender, B. Brijs, S. van Elshocht, M. Jurczak, J. Van Houdt, and D. J. Wouters, *Microelectron. Eng.*, **86**, 1789 (2009).
21. V. Longo, N. Leick, F. Roozeboom, and W. M. M. Kessels, *ECS J. Solid State Sci. Technol.*, **2**(1), N15 (2013).
22. V. Longo, N. Leick, F. Roozeboom, and W. M. M. Kessels, *ECS Trans.*, **41**(2), 63 (2011).
23. B. J. Kooi and J. T. De Hosson, *J. Appl. Phys.*, **95**, 4714 (2004).
24. V. Y. Kolosov and A. R. Thölén, *Acta Mater.*, **48**, 1829 (2000).
25. P. Favia, M. Bargallo Gonzales, E. Simoen, P. Verheyen, D. Klenov, and H. Bender, *J. Electrochem. Soc.*, **158**, H438 (2011).
26. Powder Diffraction File, Card No 35-0734, International Centre for Diffraction Data, Newton Square, PA.